Revised Manuscript with no changes marked

Improving wave energy conversion performance of a floating BBDB-OWC system by using dual chambers and a novel enhancement plate

Wenchuang Chen[a, b], Weixin Xie[a], Yongliang Zhang[b,*], Chen Wang[b,*], Liguo Wang[c], Luofeng Huang[d]

[a] School of Civil Engineering, Sun Yat-Sen University, and Southern Marine Science and Engineering Guangdong Laboratory (Zhuhai), Zhuhai, 519082, China

[b] State Key Laboratory of Hydroscience and Engineering, Tsinghua University, Beijing, 100084, China

[c] School of Marine Engineering and Technology, Sun Yat-Sen University, Zhuhai, 519082, China

[d] School of Water, Energy and Environment, Cranfield University, Cranfield MK43 0AL, UK

Abstract

In this study, a novel floating dual-chamber backward bent duct buoy oscillating water column (BBDB-OWC) wave energy converter (WEC) is introduced, featuring a horizontal plate at the bottom of the front chamber to act as an enhancement plate. A three-dimensional computational fluid dynamics (CFD) model is developed and validated by comparing its results with existing experimental measurements. The validated model is employed to investigate the hydrodynamic performance and power generation characteristics of the dual-chamber BBDB-OWC WEC under various conditions, including variations in the length of the horizontal plate (l_p/l_f) and different regular wave conditions. Key performance metrics, including peak to average ratio of power (PTARP), wave energy capture width ratio (ξ_{total}), and its wave period respond bandwidth (indicated by $P_{\xi total > 0.5}$ and $P_{\xi total > 0.7}$), are analyzed and compared with those of a traditional single-chamber BBDB-OWC WEC. The results reveal that, compared to the single-chamber WEC, the dual-chamber WEC with a specific horizontal plate length reduces the average PTARP from 2.88 to a minimum value of 1.82 for $l_p/l_f = 0.5$, improves the average ξ_{total} from 0.55 to a maximum value of 0.64 for $l_p/l_f = 2.5$, and increases $P_{\xi total > 0.5}$ and $P_{\xi total > 0.7}$ from 71% and 14% to maximum values of 86% and 43% for $l_p/l_f = 2.5$, respectively. An explanation for these observations is also provided in the context of structure motion and flow fields.

Keywords: Wave energy; Backward bent duct buoy (BBDB); Dual-chamber; Enhancement plate; Peak to average ratio of power; Capture width ratio.

* Corresponding author.

E-mail address: chenwch37@mail.sysu.edu.cn (**W. Chen**); xiewx23@mail2.sysu.edu.cn (**W. Xie**); yongliangzhang@mail.tsinghua.edu.cn (**Y. Zhang**); cqhf@mail.tsinghua.edu.cn (**C. Wang**); wanglg7@mail.sysu.edu.cn (**L. Wang**); Luofeng.Huang@cranfield.ac.uk (**L. Huang**)

1. Introduction

With the rapid advancement of the economy, humankind is consuming the Earth's finite fossil energy resources at an unprecedented pace. Consequently, the development of new energy sources has become a crucial component of various countries' energy strategies [1]. Wave energy is one of the most promising marine renewable energy sources, primarily due to its higher energy density when compared to other renewable sources such as wind and solar energy. The immeasurable potential of wave energy has motivated numerous researchers to focus their efforts on exploring methods to harness this valuable and clean energy resource [2].

According to their working principles, common wave energy converters (WECs) include oscillating water column (OWC) devices, oscillating body (OB) devices, and overtopping devices. Among these, the OWC devices stand out as one of the most promising WECs. This is due to their simple structure, straightforward power generation principle, and the advantage of their energy conversion system avoiding direct contact with seawater, resulting in relatively lower maintenance costs [3, 4]. Since the proposal of the OWC WEC, numerous scholars have conducted extensive theoretical, experimental, and numerical research to enhance its performance [5]. However, despite these efforts, the commercial application of OWC WECs has not yet been realized due to their high generation costs and relatively low efficiency. To address these challenges, some researchers have suggested installing the OWC system on marine engineering structures to improve their survivability and reduce economic costs [6-14]. Another approach involves integrating the OWC system with other WECs, such as OB devices, to increase overall power generation and compensate for the shortcomings of OWC WECs [8, 15-18]. The exploration of innovative methods to overcome the existing limitations of OWC WECs remains a key research direction.

In the aforementioned context, the dual-chamber OWC WEC has been proposed. Compared to single-chamber devices, the dual-chamber OWC WEC not only increases the overall power generation capacity, but also benefits from the mutual interaction between the device geometry and the chambers, resulting in the presence of multiple resonance periods for energy absorption and extending the operational range [19-23]. Additionally, the dual-chamber OWC WEC exhibits a more stable electricity

output curve, leading to a reduction in the load on the turbine generator, which could potentially improve the generator efficiency [20]. Consequently, researchers have increasingly focused on investigating dual-chamber and multi-chamber OWC WECs.

Rezanejad et al. [21] employed the matched characteristic functions and boundary integral analysis to examine the hydrodynamic performance of dual-chamber fixed-benthic OWC WECs with stepped bottoms. The results highlight a significant improvement in wave energy conversion efficiency attributed to the stepped bottom design. Ning et al. [24, 25] conducted both experiments and numerical simulations to analyze the performance of fixed dual-chamber OWC WECs. The results indicate that, within the chosen range of wave conditions, the rear chamber absorbs a greater amount of wave energy compared to the front chamber. He et al. [26] investigated the effect of wave frequency, front wall draft, water depth, and chamber parameters on the wave energy harvesting of offshore floating dual-chamber OWC WECs. They found that the front chamber plays a dominant role in energy capture and differs from that of fixed dual-chamber OWC WECs. Recently, Rezanejad et al. [27] proposed a new type of dual-chamber OWC WEC combined with the backward bent duct buoy (BBDB) WEC. Through numerical simulations, the device was shown to achieve a maximum capture width ratio (CWR) of over 70% under real ocean wave periods. Their experimental results indicate that a high-damping for the power take-off (PTO) system of the front chamber improves the energy capture efficiency of the device under low-frequency wave conditions. Rezanejad and Guedes Soares [28] further discovered that the interaction between the front and rear chambers significantly enhances the wave energy capture performance of the device, with each chamber dominating the energy capture process under specific wave periods. Gadelho et al. [29] analyzed the heave, pitch, and roll motions of the dual-chamber OWC WEC [27], and determined the corresponding response amplitude operator (RAO). The study also explored the relationship between the device's motion responses and wave energy capture. Xu et al. [30, 31] conducted experimental studies on the motion responses and wave energy conversion efficiency of dual-chamber OWC WECs under different flexible mooring systems. They found that the effect of the mooring system on the OWC WEC's energy conversion performance primarily depends on wave height.

The use of compact anchor designs can significantly improve the device's wave energy conversion efficiency of the device.

The floating dual-chamber OWC WEC, under the combined action of multi-degree-of-freedom motion and mooring systems, exhibits increased complexity in dynamic responses while offering a greater potential for enhanced wave energy conversion efficiency. However, to the best of the author's knowledge, research on floating dual-chamber OWC WECs is still relatively limited, and there is a lack of comprehensive understanding regarding the factors influencing the device's wave energy conversion efficiency. Additionally, there is a shortage of comparisons made with traditional floating single-chamber BBDB devices. In this study, a new floating dual-chamber BBDB-OWC WEC is proposed, consisting of a front chamber with a horizontal plate and a BBDB serving as the rear chamber. To investigate the nonlinear interaction between waves and the dual-chamber BBDB-OWC WEC, a numerical model is established based on the Navier-Stokes equations. Through a set of simulation results under regular wave conditions, this study reveals the influence of the horizontal plate on the wave energy conversion performance and the motion response of the dual-chamber BBDB-OWC WEC. Additionally, a comparison of the wave energy conversion performance is made between the dual-chamber BBDB-OWC WEC and the single-chamber BBDB.

The article is structured as follows: Section 2 presents the structural diagrams and design parameters for the dual-chamber BBDB-OWC WEC. Section 3 elaborates on the establishment and validation of the computational model. Section 4 presents systematic computational simulations in various environmental conditions and analyses the simulation results. Finally, Section 5 draws conclusions.

2. A new floating dual-chamber BBDB-OWC WEC

Fig. 1 depicts the structural diagram of a new floating dual-chamber BBDB-OWC WEC. This configuration comprises a front chamber facing the wave direction, and a rear chamber designed similarly to a single-chamber BBDB WEC. A horizontal plate is installed beneath the front chamber. In previous studies on both fixed single-chamber OWC WECs and floating BBDB WECs, it has been demonstrated that this horizontal plate improves wave energy conversion efficiency [22, 32, 33]. The

WEC is connected to the seabed by an anchor chain, which is considered an elastic, quasi-stationary catenary. It is crucial to underscore that this study does not incorporate a real turbine. Instead, the non-linear PTO damping, induced by an impulse air turbine, is simulated through the inclusion of orifices on the top wall of each chamber, as detailed in previous research [23, 26, 34]. In this paper, a Cartesian coordinate system is utilised, specifically the *O-xyz* coordinate system, see Fig. 1. This coordinate system adopts the origin as the centre of the front wall of the L-shaped duct at the equilibrium state of the WEC. The *x*- and *y*-axes are oriented in the longitudinal and transverse directions respectively when the instrument is at rest, while the *z*-axis is oriented vertically. The incident wave propagates in the *x*-direction. Due to the symmetry, it is assumed that the WEC only heave, surge and pitch.

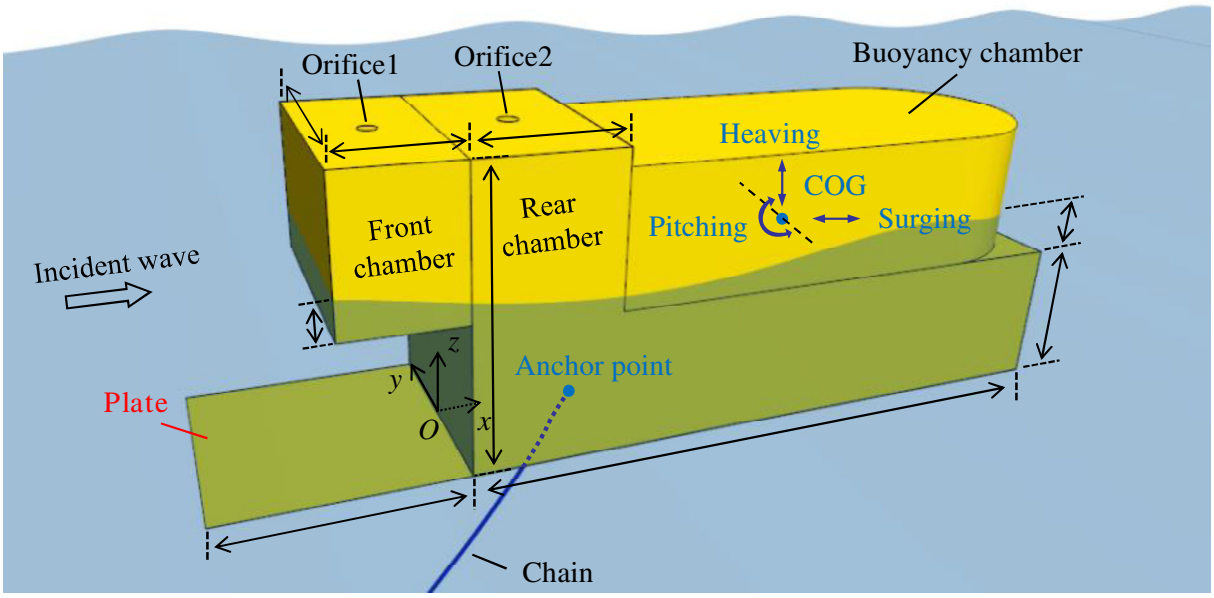

(a)

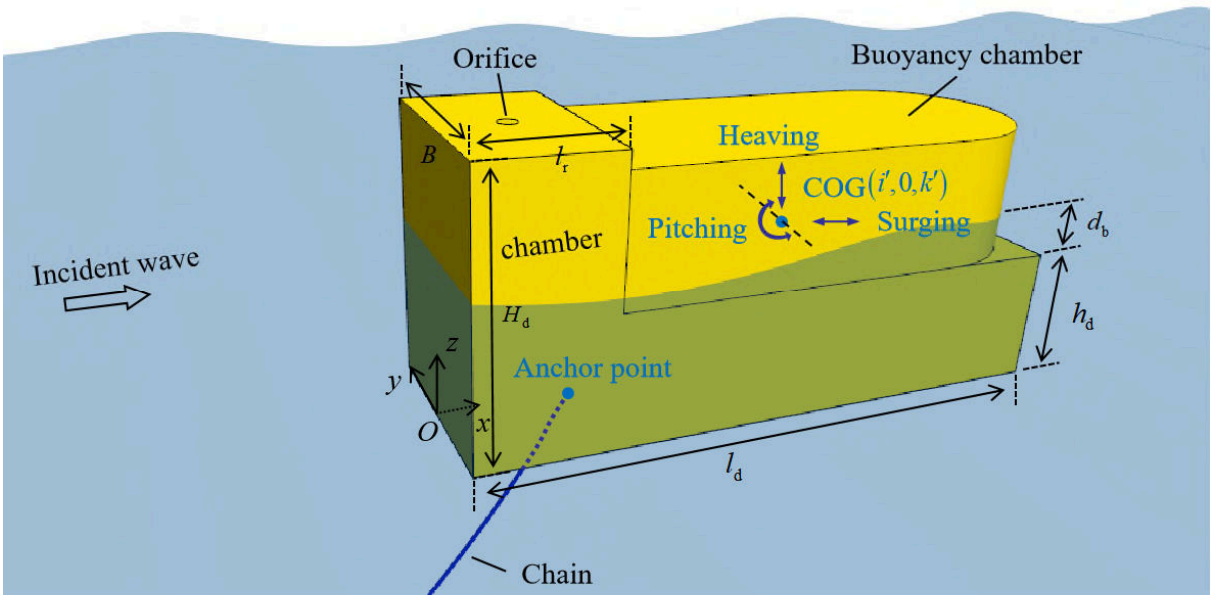

(b)

Fig. 1. Schematic of BBDB-OWC WEC: (a) Dual-chamber; (b) Single-chamber.

The design parameters for both dual-chamber and single-chamber BBDB-OWC devices are presented in Table 1. Sheng [35] suggested equal chamber length and horizontal duct height for enhanced wave energy absorption, so this form is adopted in this paper. To reduce energy dissipation during six degree of freedom motion of the floating buoy, its tail is semi-cylindrical. The rear chamber design of the dual-chamber BBDB-OWC WEC is consistent with the single-chamber BBDB device and keeps the parameters identical. The horizontal plate length l_p ranges from 0 to 3 times the front chamber length l_f. The centre of gravity (COG), mass, and moment of inertia of the dual-chamber WEC vary with l_p. The COG of the dual-chamber WEC ranges from (10.44, 0, 4.31) to (10.55, 0, 4.34), which is slightly different from the COG of the single-chamber WEC, (10.57, 0, 4.34). The mass of the dual-chamber WEC varies from 84.89 to 85.54 t, which is slightly greater than the mass of the single-chamber WEC at 84.80 t. Moreover, the moment of inertia of the dual-chamber WEC ranges from 1.41×10^6 to 1.57×10^6 kg·m^2, which is also slightly larger than that of the single-chamber WEC at 1.39×10^6 kg·m^2. Considering the scope of these differences in COG, mass, and moment of inertia, it seems reasonable to conclude that they have little impact on the hydrodynamic performance of the two WECs.

Table 1. Dimensions of the numerical model of the BBDB-OWC WEC

Parameter	Value
WEC width B	6.6 m
WEC height H_{d}	8.3 m
L-shaped duct length l_{d}	18.0 m
Duct intake height h_{d}	4.0 m
Rear chamber length l_{r}	4.0 m
Buoyancy chamber drought d_{b}	0.9 m
Front chamber length l_{f}	3.2 m
Front chamber drought d_{f}	0.7 m
Horizontal plate length $l_{\mathrm{p}}/l_{\mathrm{f}}$	0–3.0
Orifice opening ratio	1.0 %
Anchor point coordinates	(4.0, 0, 0) m
Mooring stiffness	200 kN/m
Mooring mass per meter	30.0 kg
Chain length	30.0 m
Wall thickness	0.01 m
$\mathrm{COG}(i,0,k)$	(10.44, 0, 4.31)–(10.55, 0, 4.34) m
$\mathrm{COG}(i',0,k')$	(10.57, 0, 4.34) m
Mass of dual-chamber WEC	84.89–85.54 t
Mass of single-chamber WEC	84.80 t
Moment of inertia of dual-chamber WEC	1.41×10^{6}–1.57×10^{6} kg·m^2
Moment of inertia of single-chamber WEC	1.39×10^{6} kg·m^2

3. Numerical approach

3. 1. Governing equations

As the investigated OWC WEC is of a large scale, it is important to consider the compressibility of air when predicting the device's wave energy conversion performance [36-38]. Therefore, a compressible model is adopted. Based on the viscous flow theory, the integral forms of the continuity equation and the Navier-Stokes equations are used to describe the motion of compressible fluid flows, as shown below:

$$\frac{d}{dt}\left(\int_{CV}\rho dV\right)+\int_{A}\mathbf{n}\cdot\rho\mathbf{v}\,d\boldsymbol{A}=0 \tag{1}$$

$$\frac{d}{dt}\left(\int_{CV}\rho\mathbf{v}dV\right)+\oint_{A}\mathbf{n}\cdot\rho\left(\mathbf{v}\otimes\mathbf{v}\right)d\boldsymbol{A}=\oint_{A}\mathbf{n}\cdot\left(\mathbf{T}-p\mathbf{I}\right)d\boldsymbol{A}+\int_{CV}\rho\mathbf{S}dV \tag{2}$$

In these equations, CV is the Control volume; ρ denotes the fluid density; $\boldsymbol{A}$ is the surface of the control volume; $\mathbf{n}$ is the local unit normal vector of the surface element $d\boldsymbol{A}$; $\mathbf{v}$ represents the velocity of the fluid; p is the pressure of the fluid; $\mathbf{I}$ is the identity tensor; $\mathbf{S}$ represents the body forces, such as gravity; $\mathbf{T}$ is viscous part of the stress tensor, and its calculation is based on the shear stress transport (SST) *k*-*ω* turbulence model [39].

The ideal gas equation of state is introduced to describe the gas.

$$p=\rho_{\mathrm{g}}RT_{\mathrm{a}} \tag{3}$$

Where ρ_{g} is gas density; R is the molar gas constant; T_{a} is the absolute temperature of the gas, which is assumed to be 293K.

The volume of fluid (VOF) method [40] is adopted to capture the free surface. Within each spatial mesh cell containing both air and water, the phase volume fraction is introduced and defined as follows:

$$\alpha_i=\frac{V_i}{V} \tag{4}$$

Where V_i is the volume of the *i*-th phase in the mesh cell, V is the volume of the mesh cell:

$$\sum_{i=1}^{2}\alpha_i=1 \tag{5}$$

$$\frac{\partial V_i}{\partial t}+u_j\frac{\partial V_i}{\partial x_j}=0 \tag{6}$$

Based on Newton's second law, the translational equation of motion for the WEC is given as

$$m\frac{d\mathbf{v}_{\mathrm{d}}}{dt}=\mathbf{F}_{\mathrm{f}}+\mathbf{F}_{\mathrm{m}}-m\mathbf{g} \tag{7}$$

Where m is the mass of the WEC; $\mathbf{v}_{\mathrm{d}}$ is the translational velocity of the WEC's COG; $\mathbf{F}_{\mathrm{f}}$ is the forces exerted by the fluid on the WEC; $\mathbf{F}_{\mathrm{m}}$ is the mooring forces determined using the quasi-static catenary model [41]; $\mathbf{g}$ is the gravitational acceleration. The rotational equation of motion is given as

$$J\frac{\mathrm{d}\omega_{\mathrm{d}}}{\mathrm{d}t}=M_y+M_{\mathrm{m}} \tag{8}$$

Where J is the moment of inertia about the *y*-axis relative to the COG; ω_{d} is the angular velocity of the rigid body's rotation; M_y is the moment exerted by the fluid on the WEC's COG in the *y*-direction; M_{m} is the mooring moment acting on the WEC's COG in the *y*-direction, obtained by taking the cross product of the vector from COG to the ahchor point and $\mathbf{F}_{\mathrm{m}}$.

The motion of the WEC and the fluid is fully coupled by the velocities and pressures at the fluid-structure interface, with additional constraints to ensure that fluid particles adhere to it

$$\mathbf{v}_{\mathrm{s}}^{n} = \mathbf{v}^{n} \quad \text{on } S \tag{9}$$

$$\mathbf{F}_{\mathrm{s}}^{n} + \mathbf{F}_{\mathrm{f}}^{n} = 0 \quad \text{on } S \tag{10}$$

where S is the fluid-structure interface; $\mathbf{v}_{\mathrm{s}}^{n}$ is the velocity vector of the WEC at the interface; $\mathbf{F}_{\mathrm{s}}^{n}$ represents the vector of traction applied to the WEC on the interface; and $\mathbf{F}_{\mathrm{f}}^{n}$ denotes the vector of stresses experienced by the fluid at the fluid-structure interface.

3. 2. Computational model setup

To investigate the interaction between waves and the floating dual-chamber BBDB-OWC WEC, a three-dimensional numerical wave tank (NWT) is established using the computational fluid dynamics (CFD) software Star-CCM+ in this study, as shown in Fig. 2. Previous studies have shown that the well-tested Star-CCM+ numerical model is reliable in ocean wave generation simulation and the prediction of the hydrodynamic performance of WECs [19, 42, 43]. The total length of the NWT is adjusted in accordance with the wave periods tested in this study, and fixed at 12 wavelengths. Prior to the dual-chamber OWC WEC, the length is 5 wavelengths, while it is 7 wavelengths thereafter. This arrangement facilitates the data collection from 10 wave periods before any interaction occurs between the incident wave and the reflected wave from the inlet boundary. The inlet boundary is situated on the left end of the wave tank, and fifth-order Stokes wave theory [44] is employed for wave generation. The right end of the wave tank is a pressure outlet. A damping zone of 2 wavelengths in length is implemented prior to the outlet boundary. The NWT has a height of 40 meters, with 20 meters dedicated to the water phase and 20 meters to the air phase. The bottom and sides are assigned no-slip wall boundary conditions, and the top pressure outlet is set as a constant-pressure boundary (equal to 1 atmospheric pressure). To

improve computational efficiency, we use a symmetry plane at the xOz plane, as WEC displays axisymmetric hydrodynamic. The width of the NWT is sufficiently large (5 times the device width) to reduce the influence of sidewall effects [45, 46].

The use of the overlapping grid method [47] is illustrated in Fig. 2, which incorporates two sets of grids: the background grid and the overset grid. The grid cells for the NWT have hexahedral shapes, forming the background grid. To ensure accuracy, we allocate at least 50 cells per wavelength in the x-direction of the free surface zone, with the maximum cell size in y-direction set to $\Delta y = 4\Delta x$, where Δx is the cell size in x-direction. Additionally, at least 20 cells per wave height are allocated in the z-direction. The overset area includes both the WEC and the neighboring fluid zone. This area is meshed with a fine mesh, with resolution determined through mesh convergence analysis as exemplified in Section 3.4.2. During simulation, the overset grid moves with the WEC, while the background grid remains stationary. The two grids are coupled through data exchange between accepting and donating cells. To ensure dependable data exchange, the scales of the background and overset grids around the

overlapping boundary are kept similar. For temporal discretization, a time step of 1/1000 the wave period is selected, with CFL numbers varying between 0.01 and 0.12 throughout the study. The cell sizes and time step used in this study are in accordance with the recommended values [9, 48, 49].

The simulation employs the SIMPLE scheme to couple pressure and velocity, along with a second-order implicit time discretization scheme, the Gauss-LSQ gradient discretization scheme, and a second-order upwind convection term discretization scheme. Furthermore, to accurately capture the free surface, the high-resolution interface capturing (HRIC) method is employed.

3. 3. Data monitoring

The air pressure, airflow rate and oscillating water level of chambers, as well as the heave, surge, and pitch motions of the WEC are monitored and described by the response amplitude operator (RAO) as follows:

$$\mathrm{RAO} = \frac{a}{A} \tag{11}$$

Where a is the response amplitude of the WEC during its movement; A is the amplitude of the incident wave.

Air pressure within the front and rear chambers, denoted as p_1 and p_2, is monitored using specific pressure monitoring points. There are 15 monitoring points evenly distributed throughout each chamber, as illustrated in Fig. 2. The air pressure in each chamber is determined by calculating the average value of these monitoring points. The air flow rates in both the front and rear chambers, identified as Q_1 and Q_2, are measured by integrating the vertical air velocity over a designated airflow monitoring surface located at the orifice of each chamber. Additionally, the oscillating water levels in both the front and rear chambers, denoted as η_1 and η_2, are monitored using virtual wave gauges installed within each chamber.

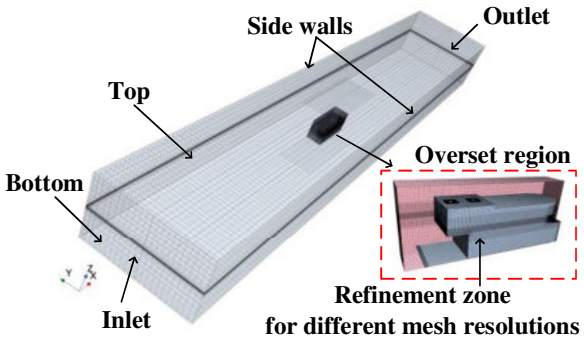

(a)

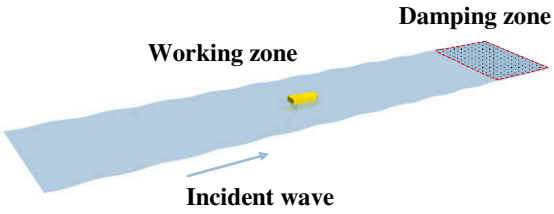

(b)

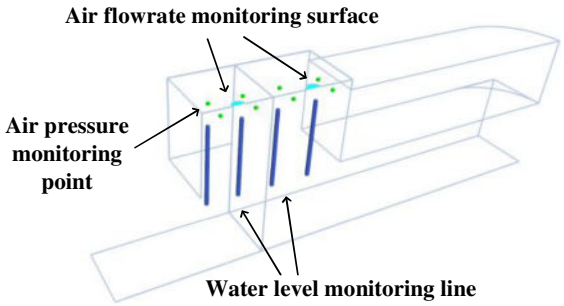

(c)

Fig. 2. Computational domain: (a) 3D numerical wave tank; (b) WEC in the simulated wave; (c) Data monitoring setup for air pressure, air flow rate and oscillating water level inside the dual chambers.

The average pneumatic power P of the individual chamber in the dual-chamber BBDB-OWC WEC can be obtained from the following formula:

$$P_i = \frac{\int_{t_0}^{t_0+t_n} p_i(t) Q_i(t)\, dt}{t_n}, i = 1,2 \tag{12}$$

Where i=1,2 denotes the front and rear chamber respectively; t_0 is the time at which the WEC's power tends to stabilize; t_n is the time interval used to analyze the power, which is chosen to be $t_n = 5T$.

The total average pneumatic power of the dual-chamber BBDB-OWC WEC is

$$P_{\text{total}} = P_1 + P_2 \tag{13}$$

According to Airy wave theory, the incident wave energy per unit width can be defined as:

$$P_{\text{in}} = \frac{\rho g H^2 \omega}{16\boldsymbol{k}} \left[1 + \frac{2\boldsymbol{k}h}{\sinh(2\boldsymbol{k}h)} \right] \tag{14}$$

The capture width ratio of each chamber is calculated as follows:

$$\xi_i = \frac{P_i}{P_{\text{in}} B}, i = 1,2 \tag{15}$$

Where B is the device width. The total capture width ratio ξ_{total} is as follows:

$$\xi_{\text{total}} = \xi_1 + \xi_2 \tag{16}$$

3. 4. Model validation

This section validates the generated wave in the NWT, and then compares the numerical results with existing experimental results [4, 33] concerning the hydrodynamic characteristics of OWC WECs. It is important to note that experimental results are not yet available for the new dual-chamber BBDB-OWC WEC. Therefore, we utilize a fixed single-chamber OWC WEC with a bottom horizontal plate (as described in [33]), which is similar to the front chamber of the current WEC, and a floating single-chamber BBDB device (as described in [4]) to conduct a numerical model-to-experiment comparison.

The normalized root mean square deviation (NRMSD) is utilized to compare results and is computed using the following equation:

$$\mathrm{NRMSD} = \frac{\sqrt{\frac{1}{N}\sum_{i=1}^{N}\left(x_i - y_i\right)^2}}{x_{\max} - x_{\min}} \tag{17}$$

Where N is the number of data points; x_i represents data from the experiments or numerical simulations of finest mesh in the convergence analysis; y_i pertains to the compared data corresponding to x_i, $x_{\max}$ and $x_{\min}$ is the maximum and minimum values of x_i.

3. 4. 1. Validation of wave-making performance of NWT

A comparison is conducted between the experimental wave data from [33] and the numerical results of the present model. The dimensions of the NWT and the positions of wave gauges can be found in [33]. As depicted in Fig. 3, the numerical model reasonably predicts wave height, wave frequency, and wave shape, with the NRMSD of the three water levels being 5.13% and 3.90% compared to experimental data and numerical data of [33] at wave period T = 1.0 s, and 5.10% and 9.86% at wave period T = 2.6 s, respectively. This indicates good agreement with the experimental results. This successful validation substantiates the NWT's capability to generate waves for subsequent research.

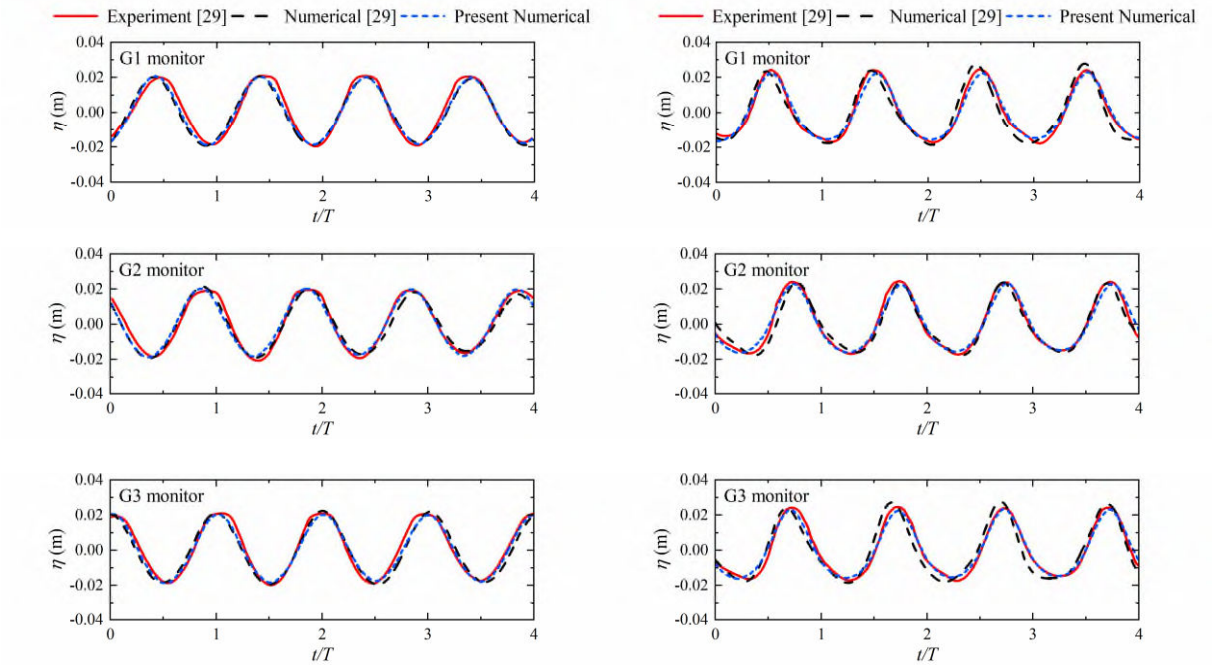

(a) (b)

Fig. 3. Comparison of the numerical and experimental results for wave-making: (a) T = 1.0 s; (b) T = 2.6 s.

3. 4. 2. Comparison of numerical and experimental hydrodynamic performance

The hydrodynamics of the OWC WEC with a bottom horizontal plate [33] and single-chamber BBDB device [4] are studied using the present model, and then compared to existing experimental results. For conciseness, the geometric parameters of these two models are not provided here. Interested readers may refer to references [33] and [4] for further details. To ensure accurate results, mesh convergence analysis is performed to identify the appropriate mesh density of the overset region. Fig. 4 shows the time series of oscillation water level and air pressure of the OWC WEC with a bottom horizontal plate under different cell sizes. Oscillation water level η and chamber air pressure p are two pivotal parameters for determining wave energy conversion efficiency. It can be seen that all cell sizes exhibit similar trends. Moreover, the fine mesh exhibits the lowest NRMSD of η and p, with values of 3.6% and 1.72% respectively when compared to the finest mesh. Considering the balance between computational accuracy and cost, the fine mesh is applied. Similar convergence tests are conducted in all subsequent simulations, consistently achieving convergence.

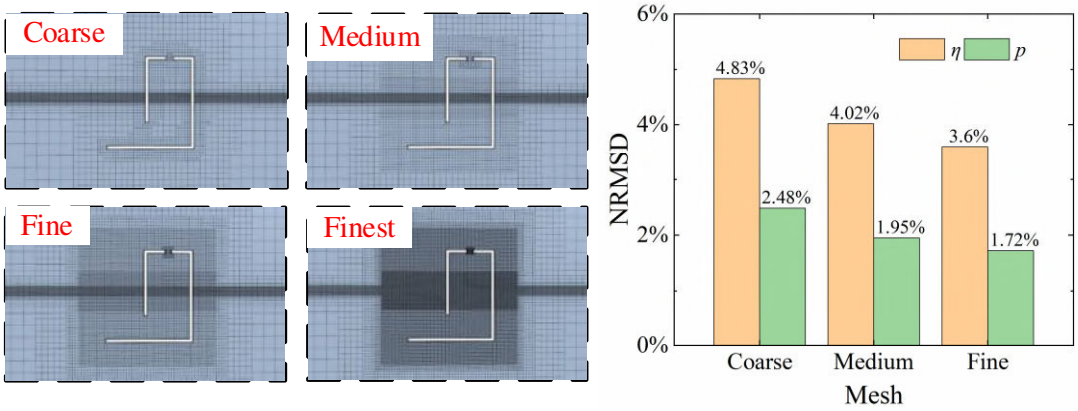

(a)

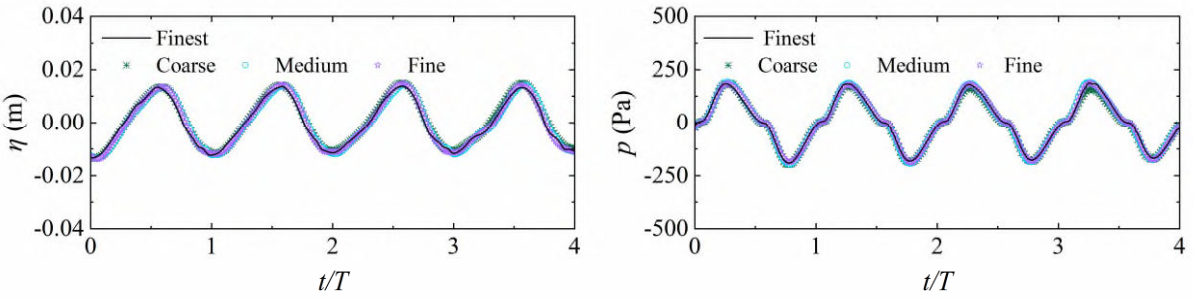

(b) (c)

Fig. 4. Results of mesh convergence: (a) different cell sizes and corresponding NRMSD; (b) free surface elevation; (c) pressure.

Fig. 5 shows the simulated time series of η and p for both the OWC WEC with a bottom horizontal plate and the single-chamber BBDB device, along with the corresponding experimental data. It can be observed that there exists an inherent discrepancy in the oscillating water level, as indicated by the NRMSD values of η for the two devices, which are 8.65% and 8.18%, respectively. This discrepancy can be expected due to its spatial non-uniformity and stochastic characteristics [45, 50, 51]. The NRMSD values of p for these two devices are 3.35% and 5.05%, respectively. Overall, the numerical results indicate satisfactory agreement with the experimental data, thereby validating the numerical model accuracy.

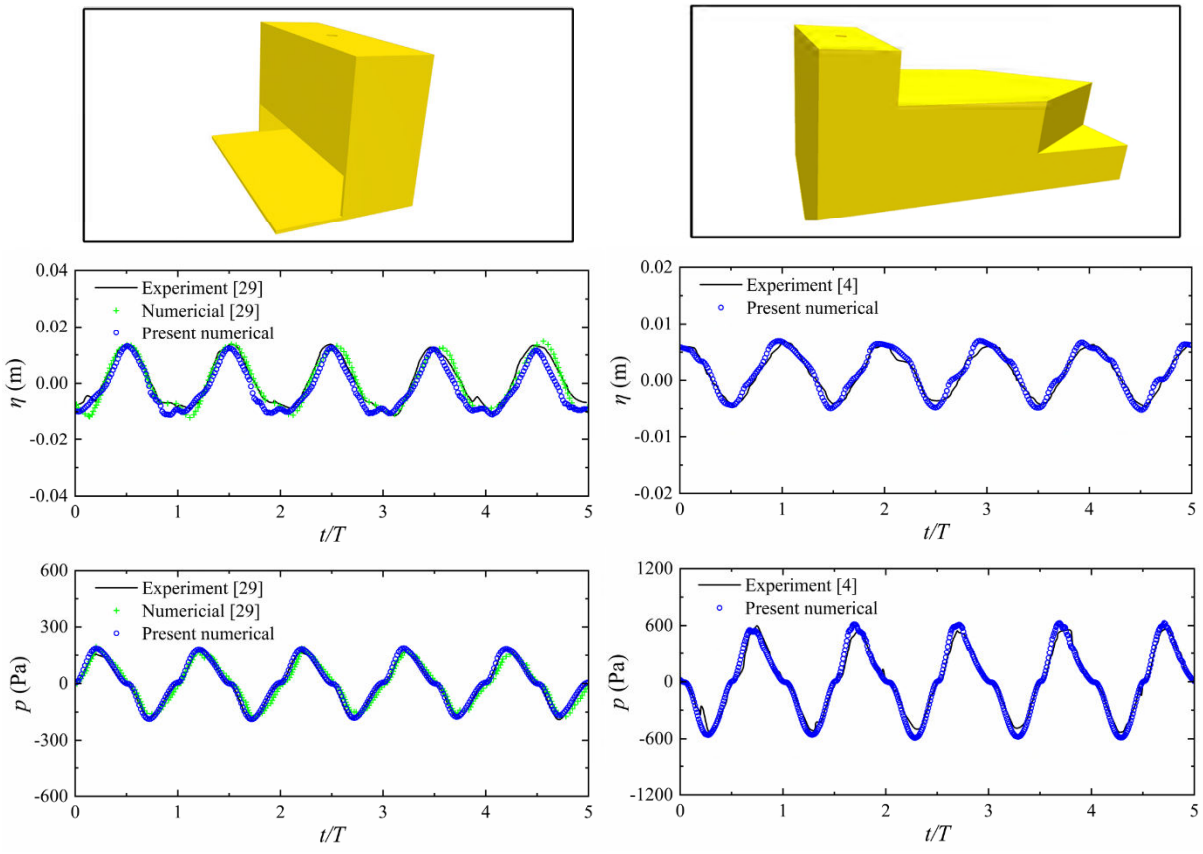

(a) (b)

Fig. 5. Comparison of numerical and experimental results: (a) Single-chamber fixed OWC WEC with a bottom horizontal plate; (b) Single-chamber BBDB-OWC WEC.

4. Results and discussion

In this section, the hydrodynamics of the dual-chamber BBDB-OWC WEC under various regular wave conditions are analyzed and compared to those of a single-chamber BBDB device. This study focuses on wave conditions in the Chinese ocean, where wave periods (T) range from 3.4 s to 6.0 s [52], with an increment of 0.2 s. The wave height (H) is fixed at 1 m, and the water depth (h) is assumed to remain constant at 20 m. A total of 112 simulation cases are carried out, and the corresponding wave condition parameters are presented in Table 2.

Table 2. Wave condition parameters

Wave period T (s)	Wave height H (m)	Water depth h (m)	Wavelength L (m)
3.4–6.0	1.0	20	18.6–55.2

4.1 Comparison of wave energy conversion performance between dual-chamber and single-chamber BBDB-OWC WECs

In this section, we will compare the overall efficiency and the peak-to-average ratio of power (indicated as PTARP) between the dual-chamber and the single-chamber BBDB-OWC WECs.

In practical wave conditions, the extraction of wave energy results in instantaneous power output that exhibits a fluctuation pattern, wherein the maximum power significantly exceeds the average power [53]. Fig. 6 displays the power output time series of different WECs for T = 4.6 s. Owing to the inherent phase difference in the hydrodynamic responses of the front and rear chambers of the dual-chamber BBDB-OWC WEC, the WEC's instantaneous power output appears to have a smaller fluctuation amplitude in comparison to the single-chamber BBDB-OWC WEC. It is worth noting that there are two different power peaks within a wave period for the single-chamber BBDB-OWC. These peaks coincide with the air compression and expansion phases inside the chamber, respectively. The uneven peak values may be attributed to the non-linearity of WEC motion, and the asymmetry of the WEC's orifice, which features a chamber on one side and an open zone on the other side. This phenomenon is also observed in [19].

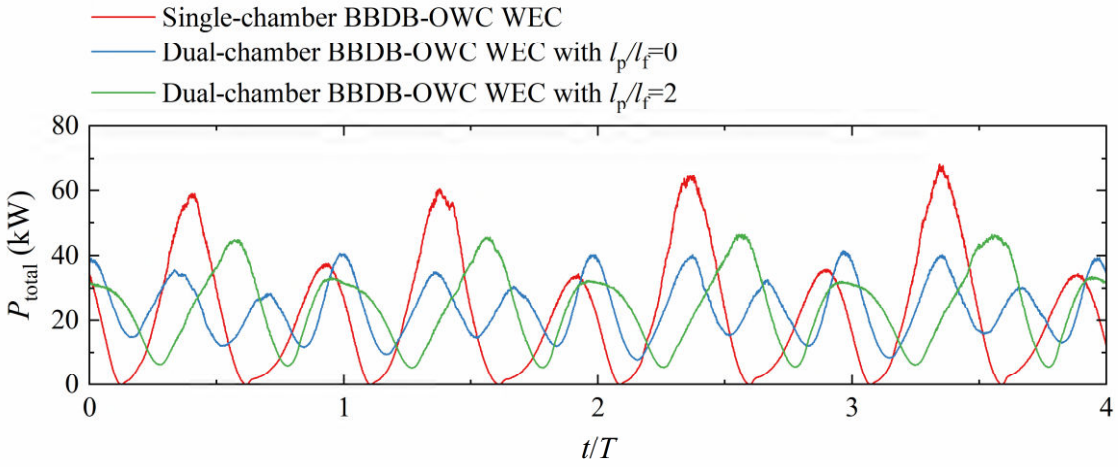

Fig. 6. Time series of P_{total} of different WECs for T = 4.6 s.

The PTARP is introduced to quantitatively characterize the instantaneous power fluctuation, which is the ratio of the highest instantaneous power to the average power. A lower PTARP value corresponds to reduced power fluctuations, making it feasible to replace costly and multi-purpose generators [54].

Fig. 7 presents the PTARP performance of different WECs. As depicted in Fig. 7a and 7b, different WECs under the examined wave conditions in this study exhibit varying PTARP values. For the single-chamber BBDB-OWC WEC, the PTARP values for all examined wave periods exceed 2.5, with the maximum value reaching 3.3 at $T = 4.8$ s. The dual-chamber BBDB-OWC WEC with various l_p/l_f have lower PTARP values than the single-chamber BBDB-OWC WEC counterpart under most wave conditions.

Fig. 7c presents the average PTARP ($PTARP_{ave}$) over the examined wave condition for dual-chamber WECs with various l_p/l_f. It is evident that the $PTARP_{ave}$ for the dual-chamber WECs ranges from 1.82 to 2.12, which is significantly lower than the $PTARP_{ave}$ value of 2.88 observed for the single-chamber WEC. Fig. 7d and 7e depict the percentage of wave periods with PTARP < 2.0 and 2.5, respectively, for different WECs. Among dual-chamber WECs, the percentage of wave periods with PTARP < 2.0, denoted as $P_{PTARP<2.0}$, ranges from 28% to 71%, while the percentage of wave periods with PTARP < 2.5, denoted as $P_{PTARP<2.5}$, ranges from 78% to 100%. Conversely, for single-chamber WEC, the percentages are 0% and 7%, respectively. These findings suggest that the dual-chamber design offers a promising approach to reducing the PTARP of OWC WECs, contributing to enhanced overall system stability and enabling the utilization of cost-effective generators to accommodate wave-induced variations [54].

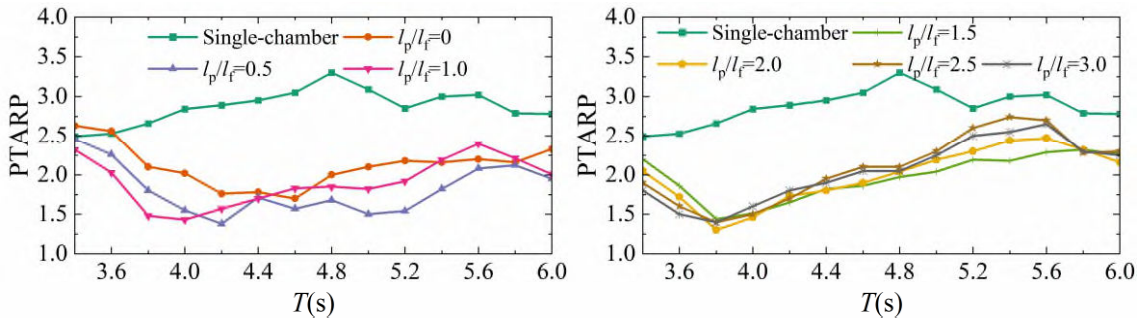

(a) (b)

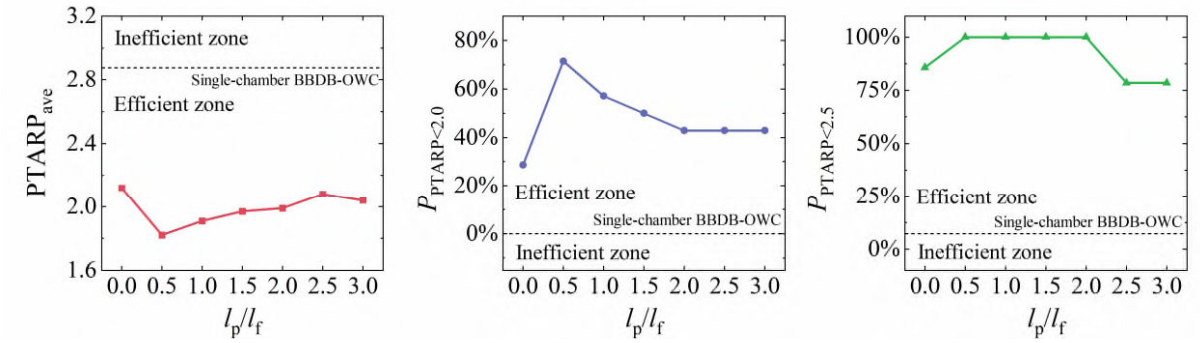

(c) (d) (e)

Fig. 7. PTARP performance of various dual-chamber WECs compared with the single-chamber WEC: (a) PTARP for l_p/l_f = 0–1.0; (b) PTARP for l_p/l_f = 1.5–3.0; (c) $PTARP_{ave}$; (d) $P_{PTARP<2.0}$; (e) $P_{PTARP<2.5}$.

Fig. 8 illustrates the capture width ratio of different OWC WECs. It can be seen in Fig. 8a and 8b that the ξ_{total} curve of the single-chamber BBDB-OWC WEC exhibits two peaks: one at T = 4.6 s, reaching 0.8, and another at T = 5.4 s, reaching 0.62. The single-chamber WEC exhibits good performance across a range of wave periods, showcasing an average capture width ratio (ξ_{ave}) of 0.55, a wave period percentage with ξ_{total} > 0.5 ($P_{\xi total>0.5}$) of 71%, and a wave period percentage with ξ_{total} > 0.7 ($P_{\xi total>0.7}$) of 14%. These results indicate that the single-chamber BBDB-OWC WEC is capable of efficiently absorbing wave energy over a wide range of wave periods.

Fig. 8a and 8b also illustrate that the incorporation of the front chamber into the single-chamber BBDB-OWC WEC, along with the inclusion of the front chamber's horizontal plate, introduces an additional peak in the ξ_{total} curve of the dual-chamber BBDB-OWC WEC. This additional peak is consistently located at approximately T = 4.0 s, regardless of the value of l_p/l_f. Under short wave conditions (T < 4.2 s), all the examined dual-chamber WECs exhibit significant efficiency improvements compared to the single-chamber WEC. In Section 4.2 and Section 4.3, we will obtain the capture width ratio curves and motion RAOs for each chamber, respectively. It is evident that the observed enhancement primarily originates from the front chamber, which will be elaborated upon in the subsequent sections. Moreover, an observation of ξ_{total} peaking at T = 4.6 s is evident for both dual-chamber and single-chamber WECs, indicating the occurrence of a resonance effect between the incident wave and the WEC's motion. Under long wave conditions ($T \geq$ 5.0 s), the ξ_{total} initially increases

with the increase of l_p/l_f. This trend continues until l_p/l_f reaches a value of 2.5, beyond which ξ_{total} ceases to increase.

Fig. 8c, 8d and 8e present the variations of ξ_{ave}, $P_{\xi total > 0.5}$, and $P_{\xi total > 0.7}$ with respect to l_p/l_f, respectively. For comparison purposes, we utilize the values obtained from the single-chamber WEC as reference lines in these figures. In the case of dual-chamber WECs with $l_p/l_f > 0.5$, ξ_{ave} surpasses that of the single-chamber WEC. For dual-chamber WECs with $l_p/l_f > 1.0$, their $P_{\xi total>0.5}$ surpasses that of the single-chamber WEC, and for all the examined dual-chamber WEC, their $P_{\xi total>0.7}$ surpasses that of the single-chamber WEC. Among these cases, the WEC with $l_p/l_f = 2.5$ performs the best, achieving ξ_{ave} of 0.64, and $P_{\xi total>0.5}$ and $P_{\xi total>0.7}$ reaching peaks of 86% and 43%, respectively. Consequently, the dual-chamber WECs with specific horizontal plate lengths exhibit both a higher wave energy capture width ratio and a wider wave period respond band than the single-chamber WEC.

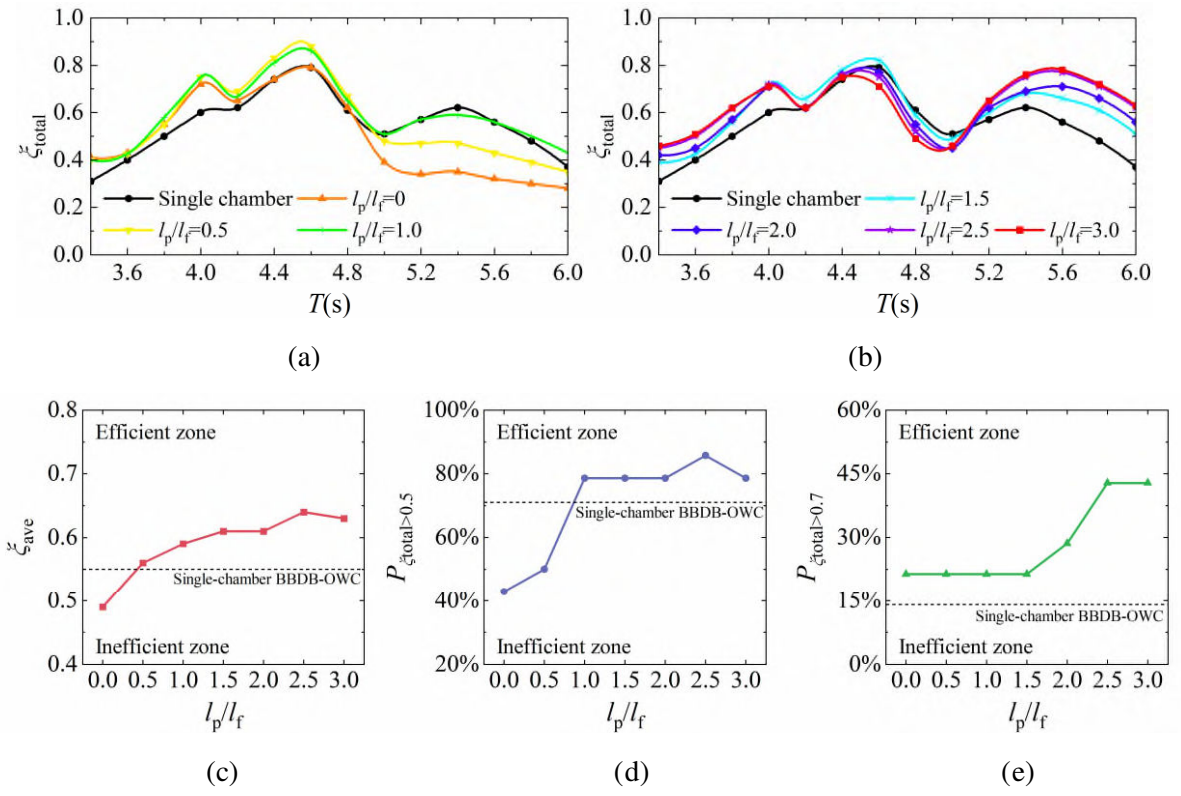

Fig. 8. Capture width ratio performance of various dual-chamber WECs compared with the single-chamber WEC: (a) ξ_{total} for l_p/l_f = 0–1.0; (b) ξ_{total} for l_p/l_f = 1.5–3.0; (c) ξ_{ave}; (d) $P_{\xi total>0.5}$; (e) $P_{\xi total>0.7}$.

To better demonstrate the difference of ξ_{total} between the single-chamber and dual-chamber WECs, a growth rate $\Delta\xi$ is defined as $\Delta\xi = (\xi_{Dual\text{-}chamber} - \xi_{Single\text{-}chamber}) / \xi_{Single\text{-}chamber}$. Fig. 9 shows the $\Delta\xi$ of dual-

chamber WECs with different l_p/l_f. For WECs with l_p/l_f = 0–1.0, $\Delta\xi$ exhibits positive values for $T \leq 4.8$ s, with a maximum value of 32%. However, $\Delta\xi$ transitions to negative values under most wave conditions when $T \geq 5.0$ s. For WECs with l_p/l_f=1.5–3.0, $\Delta\xi$ remains relatively small within the wave period range of 4.2 s $\leq T \leq$ 5.0 s. Nevertheless, beyond this wave period range, $\Delta\xi$ becomes pronounced, especially for $T \geq 5.6$ s. Therefore, it is imperative to take into account the probability of occurrence of the wave conditions of different wave periods when determining the optimal horizontal plate length to achieve a high $\Delta\xi$. In general, in regions characterized by a substantial proportion of longer wave periods ($T \geq 5.6$ s), an l_p/l_f value of 1.5–3.0 is deemed suitable. Conversely, in regions dominated by shorter wave periods ($T \leq 4.8$ s), an l_p/l_f value of 0–1.0 may be more advantageous.

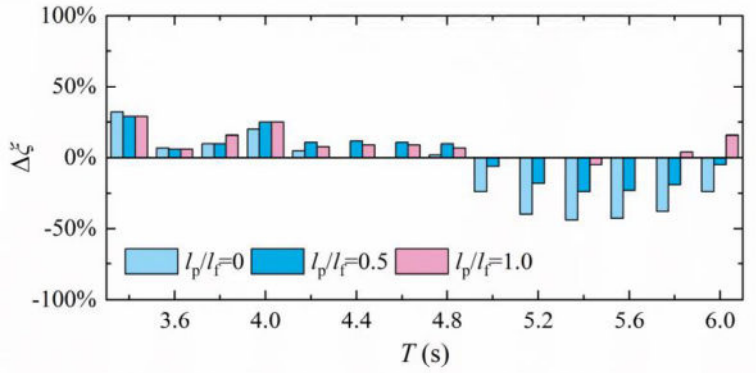

(a)

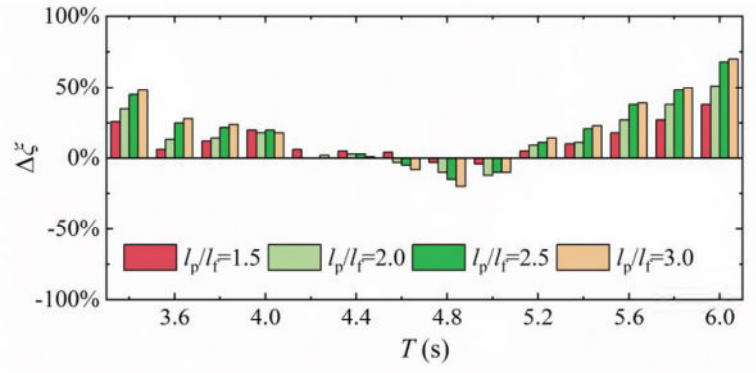

(b)

Fig. 9. $\Delta\xi$ of dual-chamber WEC with respect to single-chamber WEC for different l_p/l_f: (a) l_p/l_f = 0–1.0; (b) l_p/l_f=1.5–3.0.

4.2 Wave energy conversion performance of the front and rear chambers

Fig. 10 shows the wave energy conversion performance of the front chamber with different horizontal plate lengths. As depicted in Fig. 10a and 10b, for the WEC without the horizontal plate (i.e. $l_p/l_f = 0$), ξ_1 attains two distinct peak values of 0.44 and 0.43 at $T = 4.0$ s and 4.4 s, respectively. It is worth noting that, regardless of the value of l_p/l_f, ξ_1 exhibits two or three peaks within the considered wave period range, which is not observed in the research on fixed single-chamber OWC WECs [33].

For each of the shorter wave periods ($T < 5.0$ s), with an increase in the horizontal plate length, ξ_1 generally experiences a decline, reaches a minimum, and then slightly increases; however, it does not reach the peak values of the WEC without a horizontal plate. This observation leads to the conclusion that the front chamber with a shorter horizontal plate is more advantageous to absorb wave energy during shorter wave periods ($T < 5.0$ s). This phenomenon is further confirmed in Fig. 10c, 10d and 10e, where peaks in the RAOs of p_1, Q_1, and η_1 are all observed in the region of $0 \le l_p/l_f \le 1.0$ and 4.0 s $\le T \le$ 4.8 s. Remarkably, these three parameters exhibit the same trend in this range. This behavior can likely be attributed to the reduced motion amplitude of the dual-chamber WEC under short wave conditions, facilitating efficient wave energy absorption in the front chamber [27, 55, 56]. Conversely, for each of the longer wave periods ($T > 5.0$ s), with an increase in the horizontal plate length, ξ_1 gradually increases until it reaches a plateau value, which remains below 0.25. Notably, WECs with $l_p/l_f \ge 2.0$ exhibit prominent peaks at $T = 5.6$ s. It can be concluded that the front chamber with a longer horizontal plate length is more advantageous to absorb wave energy during longer wave periods ($T > 5.0$ s). This observation is corroborated in Fig. 10c, 10d and 10e, where peak RAOs of p_1, Q_1, and η_1 are all discernible in the region of $1.5 \le l_p/l_f \le 2.5$ and 5.4 s $\le T \le$ 5.8 s, and these three parameters exhibit analogous trend within this ranges.

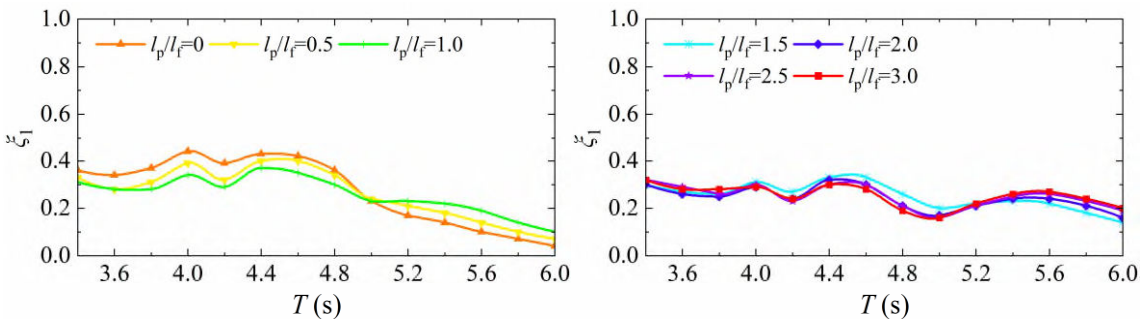

(a) (b)

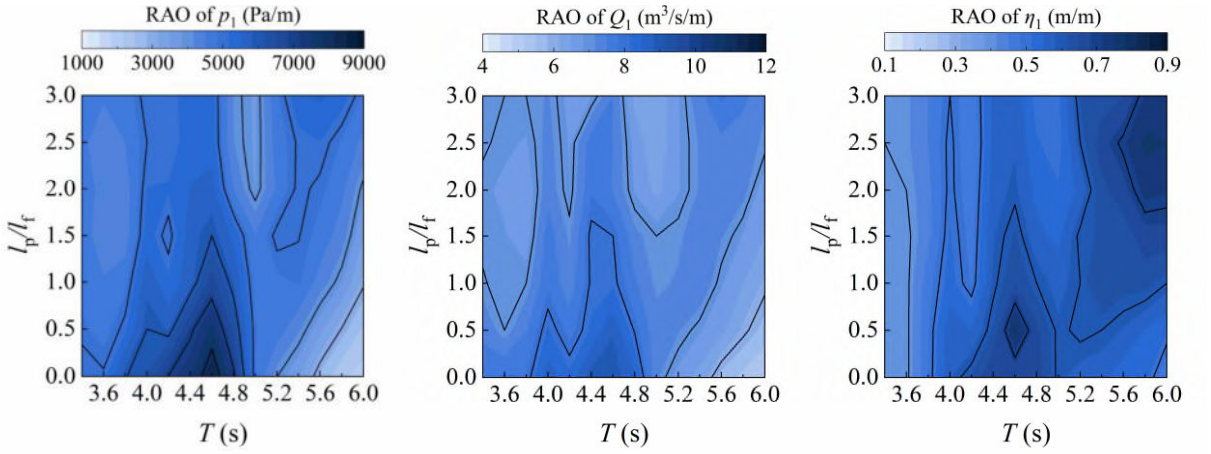

(c) (d) (e)

Fig. 10. Wave energy conversion performance of the front chamber for different horizontal plate lengths: (a) ξ_1 for l_p/l_f = 0–1.0; (b) ξ_1 for l_p/l_f = 1.5–3.0; (c) RAO of p_1; (d) RAO of Q_1; (e) RAO of η_1.

Fig. 11 illustrates the wave energy conversion performance of the rear chamber concerning varying horizontal plate lengths. ξ_2 exhibits two peaks when $l_p/l_f \leq 0.5$, and three peaks when $l_p/l_f \geq 1.0$. The WEC without a horizontal plate exhibits the lowest ξ_2 in the rear chamber. As l_p/l_f increases, ξ_2 generally improves under most wave conditions, particularly during the longer wave periods ($T > 5.0$ s). After l_p/l_f reaching 2.5, ξ_2 plateaus. In addition, the variation in horizontal plate length has little impact on the two peak values of ξ_2 which occurs when $T \leq 4.8$ s, but it has a significant impact on the peak value of ξ_2 which occurs when $T \geq 5.4$ s. Fig. 11c, 11d and 11e show the contour maps of the RAOs of p_2, Q_2, and η_2 with respect to varying l_p/l_f and T, respectively. These contour maps exhibit peaks in two regions: $0 \leq l_p/l_f \leq 3.0$, 4.4 s $\leq T \leq$ 4.6 s, and $1.0 \leq l_p/l_f \leq 3.0$, 5.4 s $\leq T \leq$ 5.8 s, which correspond to the occurrence of the two peaks in ξ_2 during 4.4 s $\leq T \leq$ 4.6 s and 5.4 s $\leq T \leq$ 5.8 s, respectively. Moreover, the RAOs of p_2, Q_2, and η_2 are nearly identical for T = 4.0 s and 4.2 s, indicating that the output power is almost equal. However, considering that the incident wave energy is smaller for T = 4.0 s, the resulting ξ_2 is larger for T = 4.0 s as per Eq. (15), thus explaining the peak at T = 4.0 s.

Overall, the rear chamber of the WECs equipped with specific horizontal plate of $l_p/l_f > 1.0$ demonstrates commendable wave energy conversion performance for $T \geq 4.0$ s (as depicted in Fig. 11). Conversely, the front chamber excels in wave energy conversion for $T \leq 4.6$ s (as shown in Fig. 10). Consequently, the dual-chamber WECs with specific horizontal plate length ($l_p/l_f > 1.0$) exhibit both a

greater wave energy capture width ratio and a broader respond band compared to the single-chamber WEC (refer to Fig. 8). Thus, the horizontal plate can be regarded as an enhancement plate that improves the wave energy capture performance of the WEC.

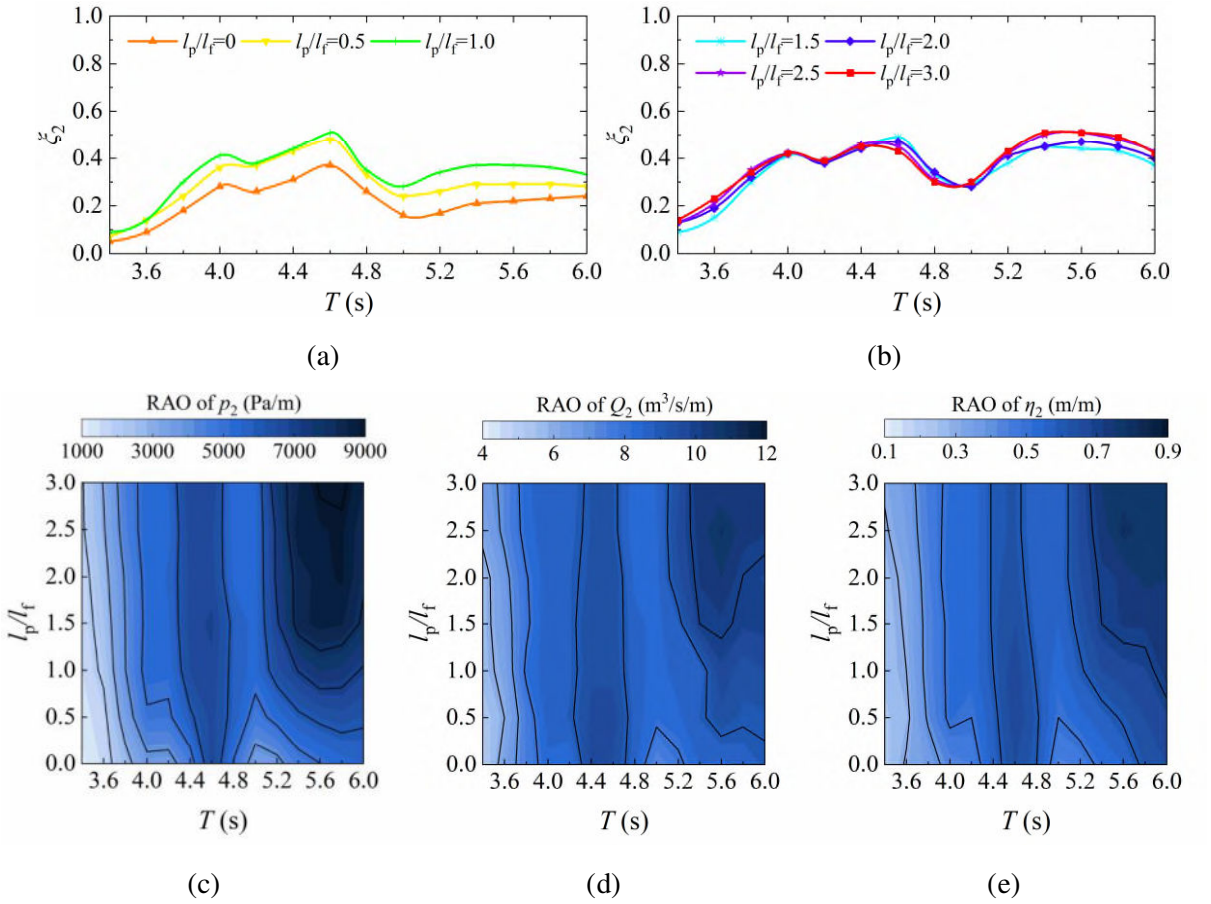

Fig. 11. Wave energy conversion performance of the rear chamber for different horizontal plate lengths: (a) ξ_2 for l_p/l_f = 0–1.0; (b) ξ_2 for l_p/l_f = 1.5–3.0; (b) RAO of p_2; (c) RAO of Q_2; (d) RAO of η_2.

4.3 Motion RAOs and flow field

Fig. 12 illustrates contour maps of surge, heave, and pitch RAOs of the dual-chamber WECs with varying horizontal plate lengths. As shown in Fig. 12a, the surge RAO exhibits two prominent peaks within two specific regions: $0 \le l_p/l_f \le 1.0$, 4.2 s $\le T \le$ 4.6 s, and $1.0 \le l_p/l_f \le 3.0$, 5.2 s $\le T \le$ 5.6 s. The two peaks coincide with the peaks observed in the contour maps of RAOs of p_1, Q_1, η_1, p_2, Q_2, and η_2 (as demonstrated in Fig. 10 and Fig. 11), accompanied by a slight shift in the resonance period. This observation indicates that surge motion plays a primary role in influencing the wave energy conversion performance of the dual-chamber WEC within the examined wave periods. In Fig. 12b and 12c, the

heave and pitch RAOs of the dual-chamber WECs with different horizontal plate lengths generally exhibit an increasing trend with an increase in wave period. For each wave period, as the horizontal plate length increases, the heave RAO shows a slight increment, while the pitch RAO gradually decreases. This behavior may be due to that as the horizontal plate length increases, the amplification of the excitation force in the device's heave direction is marginally greater than the amplification of the damping force, while the amplification of the excitation moment in the device's pitch direction is markedly smaller than the amplification of the damping moment.

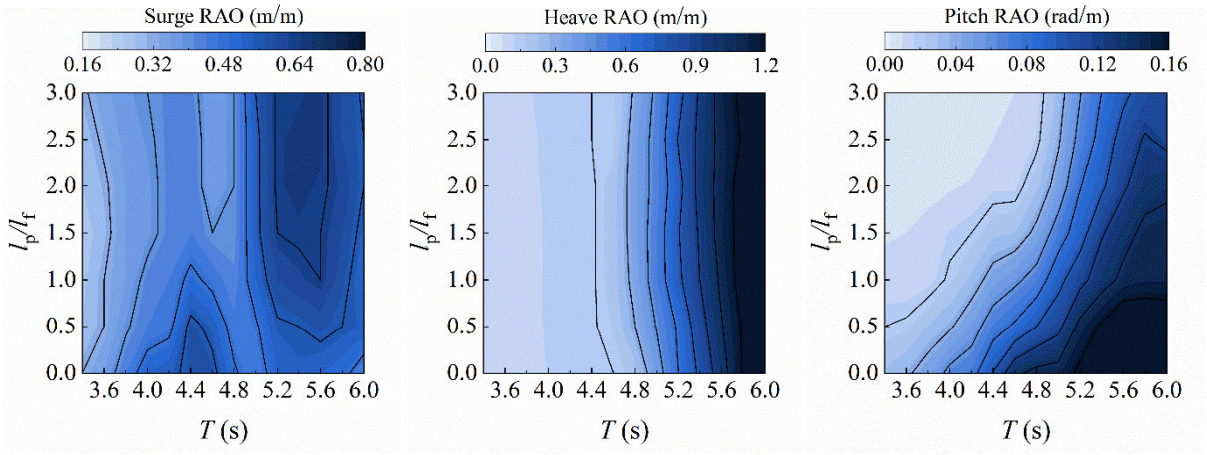

(a) (b) (c)

Fig. 12. Motion RAOs for the dual-chamber BBDB-OWC WEC with varying horizontal plate lengths: (a) Surge RAO; (b) Heave RAO; (c) Pitch RAO.

Fig. 13 displays the time series of zero-mean normalized hydrodynamic responses for three different WECs over a single wave cycle (T = 4.6 s and H = 1.0 m), while Fig. 14 provides visualizations of the water flow velocity field and the air pressure field for the same three devices during the same wave period. The time t = 0 corresponds to the moment when the rear chamber experiences its maximum air pressure.

As observed in Fig. 13, p_2 shows nearly identical response phase behavior for both the single-chamber and the two dual-chamber WECs. In contrast, p_1 exhibits a noticeable phase difference between the two dual-chamber WECs. Furthermore, there is a phase difference of approximately 0.6π and 0.4π between p_1 and p_2 for the two dual-chamber WECs. This phase difference approaching 0.5π contributes to a smoother output power, as illustrated in Fig. 6, resulting in a smaller PTARP as described in Section

4.1. In addition, it is worth noting that the three WECs display distinct response phase characteristics in surge, heave and pitch.

In Fig. 14, at t = 0, the incident wave peak reaches the front wall of the WECs, and the inflow velocity of water in the L-shaped channel of the three WECs reaches the maximum, along with the air pressure of the three chambers reaching maximum positive value. At $t = T/2$, the incident wave trough arrives at the front wall of the WECs. The outflow velocity of water in the L-shaped channel of all three WECs reaches the maximum, while the air pressure in all three chambers reaches the maximum negative value. At $t = T/4$ and $t = 3T/4$, the internal water surface of the three chambers reaches the highest and lowest level, respectively, with the air pressure approaching approximately 0. Moreover, there is a noteworthy phenomenon that turbulence occurs at the right-angle intersection of the buoyancy chamber, the opening of the L-shaped channel, and the front wall of the front chamber. Measures such as implementing a streamlined design can be employed to mitigate turbulence dissipation and enhance the absorption of wave energy. However, this topic falls beyond the scope of the present study.

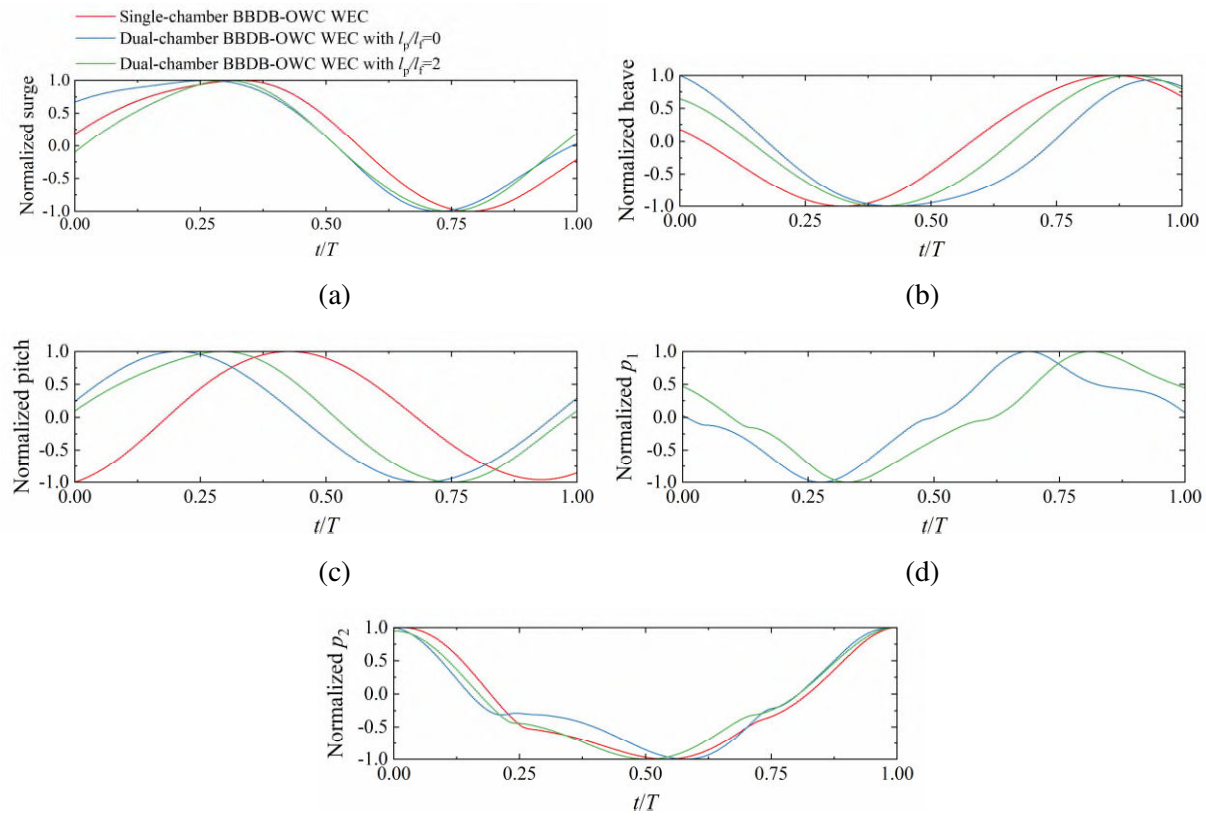

Fig. 13. Time series of the zero-mean normalized hydrodynamic responses for three different WECs within a wave period: (a) Surge; (b) Heave; (c) Pitch; (d) p_1; (e) p_2.

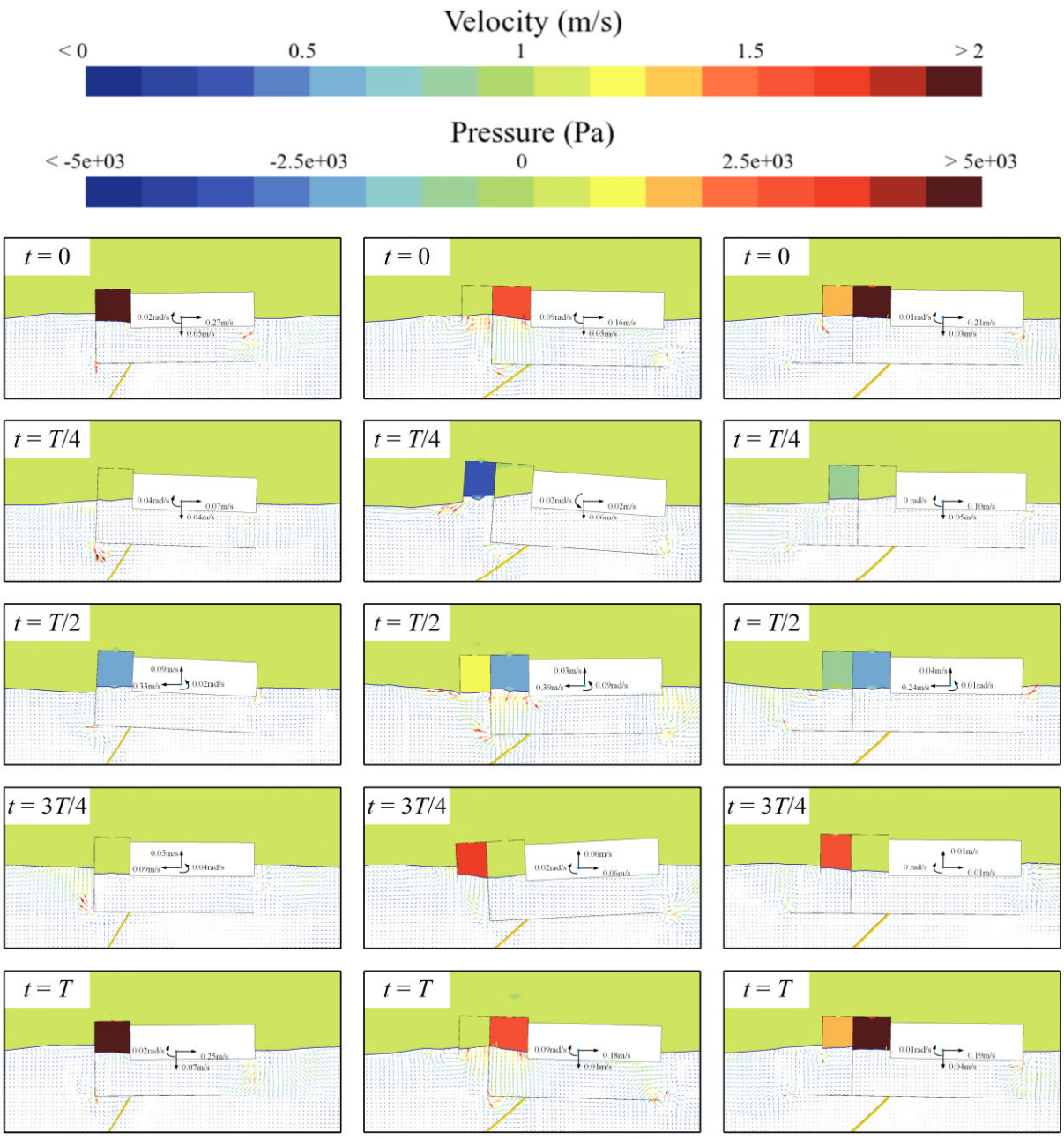

(a) (b) (c)

Fig. 14. Water flow velocity field and air pressure field at the medium longitudinal section within a wave period for three different WECs: (a) Single-chamber WEC; (b) Dual-chamber WEC without an enhancement plate; (c) Dual-chamber WEC with an enhancement plate.

5. Conclusions

In this study, a new floating dual-chamber BBDB-OWC WEC is proposed, comprising a front chamber equipped with a enhancement plate and a rear chamber in the shape of a BBDB. A three-dimensional CFD model is developed to investigate the nonlinear interaction between waves and the dual-chamber BBDB-OWC WEC. The model is validated by a good agreement between its results and existing experimental data. Subsequently, the wave energy conversion performance of the dual-chamber BBDB-OWC WEC is analyzed under various conditions, including the variation in the length of the horizontal plate and different regular wave conditions. Comparison is made with a single-chamber BBDB-OWC WEC, considering parameters such as PTARP, ξ_{total}, $P_{\xi total>0.5}$ and $P_{\xi total>0.7}$. Moreover, an analysis of the hydrodynamic characteristics of both the front and rear chambers is conducted, along with an examination of the motion RAOs and an investigation into the flow field surrounding the floating structure. The main conclusions drawn from this work are as follows:

1) Compared to a single-chamber WEC, the dual-chamber WEC with a specific enhancement plate length reduces $PTARP_{ave}$ from 2.88 to a minimum value of 1.82 for $l_p/l_f = 0.5$, improves ξ_{ave} from 0.55 to a maximum value of 0.64 for $l_p/l_f = 2.5$, and increases $P_{\xi total>0.5}$ and $P_{\xi total>0.7}$ from 71% and 14% to maximum values of 86% and 43% for $l_p/l_f = 2.5$, respectively.
2) There is a phase difference approaching 0.5π between p_1 and p_2 for the dual-chamber WECs, yielding a smoother output power, i.e., a smaller PTARP. The rear chamber of the WECs equipped with a specific horizontal plate of $l_p/l_f > 1.0$ demonstrates commendable wave energy conversion performance for $T \geq 4.0$ s. Conversely, the front chamber excels in wave energy conversion for $T \leq 4.6$ s. Consequently, the dual-chamber WECs with a specific enhancement plate length ($l_p/l_f > 1.0$) exhibit both a greater wave energy capture width ratio and a broader respond bandwidth compared to the single-chamber WEC.
3) Contour map of surge RAO with respect to horizontal plate lengths and wave periods coincide in the contour maps of RAO of p_1, Q_1, η_1, p_2, Q_2, and η_2, albeit with a slight shift in resonance period, indicating that surge motion primarily influences the wave energy conversion performance of the dual-chamber WEC within the examined wave periods.

Future work should focus on a comprehensive research approach that integrates experiments, theoretical analysis, and numerical simulations to conduct an in-depth exploration of the WEC's performance under both regular and irregular wave conditions. This has the potential to significantly enhance the commercial utilization of WECs.

Acknowledgements

Wenchuang Chen acknowledges grants received from the National Natural Science Foundation of China (Grant No. 52201349, 52311530078), Guangdong Basic and Applied Basic Research Foundation (Grant No. 2023A1515012224, 2023B1515040028), Open Research Fund Program of State key Laboratory of Hydroscience and Engineering (Grant No. sklhse-2022-B-05), and the Innovation Group Project of Southern Marine Science and Engineering Guangdong Laboratory (Zhuhai). Yongliang Zhang acknowledges the Laoshan Laboratory (Grant No. LSKJ202204503). Chen Wang acknowledges the support from the Shuimu Tsinghua Scholar Program. Liguo Wang acknowledges the National Natural Science Foundation of China (Grant No. 52101342), Guangdong Basic and Applied Basic Research Foundation (Grant No. 2022A1515010792). Luofeng Huang acknowledges the Royal Society (IEC\NSFC\223253).

Nomenclature

$\boldsymbol{A}$	Surface of the control volume
A	Amplitude of the incident wave
a	Response amplitude of the WEC
B	Width of the WEC
CV	Control volume
d_{b}	Buoyancy chamber drought of the WEC
d_{f}	Front chamber drought
$\mathbf{F}_{\mathrm{f}}$	Forces exerted by the fluid on the WEC
$\mathbf{F}_{\mathrm{f}}^{n}$	Vector of stresses experienced by the fluid at the fluid-structure interface

570	$\mathbf{F}_{\mathrm{m}}$	Mooring forces
571	$\mathbf{F}_{\mathrm{s}}^{n}$	Vector of traction applied to the WEC on the interface
572	$\mathbf{g}$	Gravitational acceleration
573	H	Wave height
574	h	Waters depth
575	H_{d}	Height of the WEC
576	h_{d}	Duct intake height of the WEC
577	$\mathbf{I}$	Identity tensor
578	i	The x-direction coordinate of center of gravity of the WEC
579	J	Moment of inertia about the y-axis relative to the COG
580	k	The z-direction coordinate of center of gravity of the WEC
581	$\boldsymbol{k}$	Wave number
582	L	Wavelength
583	l_{d}	L-shaped duct length of the WEC
584	l_{f}	Front chamber length
585	l_{p}	Horizontal plate length
586	l_{r}	Rear chamber length of the WEC
587	M_{m}	Mooring moment acting on the WEC's COG in *y*-direction
588	M_{y}	Moment exerted by the fluid on the WEC's COG in *y*-direction
589	m	Mass of WEC
590	N	Number of data points
591	$\mathbf{n}$	Local unit normal vector of the surface
592	NRMSD	Normalized root mean square deviation
593	p	Pressure of fluid
594	P_i	Average aerodynamic power of individual chamber of WEC within one wave period

595	P_{in}	Total energy flux of the incident wave per unit width
596	p_i	Pressure of *i*-th chamber
597	$P_{\mathrm{PTARP<2.0}}$	Percentage of wave periods with PTARP < 2.0
598	$P_{\mathrm{PTARP<2.5}}$	Percentage of wave periods with PTARP < 2.5
599	P_{total}	Average pneumatic power of all chambers of WEC within one wave period
600	$P_{\xi\mathrm{total>0.5}}$	Percentage of wave periods with $\xi_{\mathrm{total}} > 0.5$
601	$P_{\xi\mathrm{total>0.7}}$	Percentage of wave periods with $\xi_{\mathrm{total}} > 0.7$
602	PTARP	Peak-to-average ratio of power
603	$\mathrm{PTARP}_{\mathrm{ave}}$	Average peak-to-average ratio of power across a range of wave conditions
604	Q	Air flow rate
605	Q_i	Air flow rate of *i*-th chamber
606	R	Molar gas constant
607	RAO	Response amplitude operator
608	S	Fluid-structure interface
609	$\mathbf{S}$	Body forces
610	T	Wave period
611	$\mathbf{T}$	Viscous part of the stress tensor
612	T_{a}	Absolute temperature of the gas
613	t_0	Time at which the WEC's power output tends to stabilize
614	t_n	Time interval used to analyze the power
615	V	Volume of the mesh cell
616	$\mathbf{v}$	Velocity of the fluid
617	$\mathbf{v}_{\mathrm{d}}$	Translational velocity of the WEC's COG
618	V_i	Volume of the *i* phase in the mesh cell
619	$\mathbf{v}_s^n$	Velocity vector of the WEC at the interface

620	x_i	Data from the experiments or numerical simulations
621	$x_{\max}$	Maximum value of x_i
622	$x_{\min}$	Minimum value of x_i
623	y_i	Compared data corresponding to x_i
624	α_i	volume fraction of i-th phase
625	ρ	Fluid density
626	ρ_g	Gas density
627	ω	Wave frequency
628	ω_d	Angular velocity of the rigid body's rotation
629	ξ_{total}	Wave energy capture width ratio of the WEC
630	ξ_{ave}	Average wave energy capture width ratio across a range of wave conditions
631	ξ_i	Wave energy capture width ratio of i-th chamber
632	η	Free surface displacement
633	η_i	Oscillating water level in i-th chamber
634	Δx	Mesh cell size in x-direction
635	Δy	Mesh cell size in y-direction
636	$\Delta\xi$	Relative difference of ξ_{total} between the dual-chamber and single-chamber WECs

637 **References**

638 [1] Kolios A, Di Maio L F, Wang L, Cui L, Sheng Q H. Reliability assessment of point-absorber wave energy
639 converters. Ocean Engineering 2018;163:40-50.

640 [2] Khojasteh D, Shamsipour A, Huang L F, Tavakoli S, Haghani M, Flocard F, Farzadkhoo M, Iglesias G, Hemer
641 M, Lewis M, Neill S, Bernitsas M M, Glamore W. A large-scale review of wave and tidal energy research over the
642 last 20 years. Ocean Engineering 2023;282:114995.

643 [3] Farrok O, Ahmed K, Tahlil A D, Farah M M, Kiran M R, Islam M R. Electrical Power Generation from the
644 Oceanic Wave for Sustainable Advancement in Renewable Energy Technologies. Sustainability 2020;12.

645 [4] Wu B J, Li M, Wu R K, Zhang Y Q, Peng W. Experimental study on primary efficiency of a new pentagonal
646 backward bent duct buoy and assessment of prototypes. Renewable Energy 2017;113:774-83.

[5] Ning D Z, Wang R Q, Zou Q P, Teng B. An experimental investigation of hydrodynamics of a fixed OWC Wave Energy Converter. Applied Energy 2016;168:636-48.

[6] Astariz S, Iglesias G. The economics of wave energy: A review. Renewable and Sustainable Energy Reviews 2015;45:397-408.

[7] Cabral T, Clemente D, Rosa-Santos P, Taveira-Pinto F, Morais T, Belga F, Cestaro H. Performance Assessment of a Hybrid Wave Energy Converter Integrated into a Harbor Breakwater. Energies 2020;13.

[8] Cheng Y, Fu L, Dai S S, Collu M, Cui L, Yuan Z M, Incecik A. Experimental and numerical analysis of a hybrid WEC-breakwater system combining an oscillating water column and an oscillating buoy. Renewable & Sustainable Energy Reviews 2022;169:112909.

[9] Wang C, Xu H, Zhang Y, Chen W. Power capture analysis of a five-unit oscillating water column array integrated into a breakwater in terms of flow field visualization. Energy Conversion and Management 2023;293:117449.

[10] Reabroy R, Zheng X, Zhang L, Zang J, Yuan Z, Liu M, Sun K, Tiaple Y. Hydrodynamic response and power efficiency analysis of heaving wave energy converter integrated with breakwater. Energy Conversion and Management 2019;195:1174-86.

[11] Perez-Collazo C, Greaves D, Iglesias G. Hydrodynamic response of the WEC sub-system of a novel hybrid wind-wave energy converter. Energy Conversion and Management 2018;171:307-25.

[12] Zhang H M, Zhou B Z, Zang J, Vogel C, Jin P, Ning D Z. Optimization of a three-dimensional hybrid system combining a floating breakwater and a wave energy converter array. Energy Conversion and Management 2021;247:114717.

[13] Shahabi-Nejad M, Nikseresht A H. A comprehensive investigation of a hybrid wave energy converter including oscillating water column and horizontal floating cylinder. Energy 2022;243:122763.

[14] Masoomi M, Sarlak H, Rezanejad K. Hydrodynamic performance analysis of a new hybrid wave energy converter system using OpenFOAM. Energy 2023;269:126807.

[15] Cui L, Zheng S M, Zhang Y L, Miles J, Iglesias G. Wave power extraction from a hybrid oscillating water column-oscillating buoy wave energy converter. Renewable & Sustainable Energy Reviews 2021;135:110234.

[16] Jalani M A, Saad M R, Samion M K H, Imai Y, Nagata S, Abdul Rahman M R. Numerical study on a hybrid WEC of the Backward Bent Duct Buoy and Point Absorber. Ocean Engineering 2023;267:113306.

[17] Simonetti I, Esposito A, Cappietti L. Experimental Proof-of-Concept of a Hybrid Wave Energy Converter Based on Oscillating Water Column and Overtopping Mechanisms. Energies 2022;15.

[18] Simonetti I, Cappietti L. Hydraulic performance of oscillating water column structures as anti-reflection devices to reduce harbour agitation. Coastal Engineering 2021;165:103837.

[19] Elhanafi A, Macfarlane G, Ning D. Hydrodynamic performance of single–chamber and dual–chamber offshore–stationary Oscillating Water Column devices using CFD. Applied Energy 2018;228:82-96.

[20] Hsieh M F, Lin I H, Dorrell D G, Hsieh M J, Lin C C. Development of a Wave Energy Converter Using a Two Chamber Oscillating Water Column. Ieee Transactions on Sustainable Energy 2012;3:482-97.

[21] Rezanejad K, Bhattacharjee J, Guedes Soares C. Analytical and numerical study of dual-chamber oscillating water columns on stepped bottom. Renewable Energy 2015;75:272-82.

[22] Wang C, Zhang Y. Wave power extraction analysis on a dual-chamber oscillating water column device composed by two separated units: An analytical study. Applied Ocean Research 2021;111:102634.

[23] Wang C, Zhang Y L. Numerical investigation on the wave power extraction for a 3D dual-chamber oscillating water column system composed of two closely connected circular sub-units. Applied Energy 2021;295:117009.

[24] Ning D, Wang R, Zhang C. Numerical Simulation of a Dual-Chamber Oscillating Water Column Wave Energy Converter. Sustainability 2017;9.

[25] Ning D-z, Wang R-q, Chen L-f, Sun K. Experimental investigation of a land-based dual-chamber OWC wave energy converter. Renewable and Sustainable Energy Reviews 2019;105:48-60.

[26] He F, Leng J, Zhao X Z. An experimental investigation into the wave power extraction of a floating box-type breakwater with dual pneumatic chambers. Applied Ocean Research 2017;67:21-30.

[27] Rezanejad K, Gadelho J F M, Xu S, Guedes Soares C. Experimental investigation on the hydrodynamic performance of a new type floating Oscillating Water Column device with dual-chambers. Ocean Engineering 2021;234:109307.

[28] Rezanejad K, Guedes Soares C. Hydrodynamic Investigation of a Novel Concept of Oscillating Water Column Type Wave Energy Converter Device. Journal of Offshore Mechanics and Arctic Engineering 2021;143.

[29] Gadelho J F M, Rezanejad K, Xu S, Hinostroza M, Guedes Soares C. Experimental study on the motions of a dual chamber floating oscillating water column device. Renewable Energy 2021;170:1257-74.

[30] Xu S, Rezanejad K, Gadelho J F M, Wang S, Guedes Soares C. Experimental investigation on a dual chamber floating oscillating water column moored by flexible mooring systems. Ocean Engineering 2020;216:108083.

[31] Xu S, Rezanejad K, Gadelho J F M, Guedes Soares C. Influence of the power take-off damping of a dual chamber floating oscillating water column on the mooring fatigue damage. Ocean Engineering 2022;249:110832.

[32] Chen W, Zhang Y, Yu H, Sheng W. Experimental study on Backward Bent Duct Buoy wave energy converter with a plate. Journal of Hydroelectric Engineering 2020;39:1-9.

[33] Deng Z Z, Wang C, Wang P, Higuera P, Wang R Q. Hydrodynamic performance of an offshore-stationary OWC device with a horizontal bottom plate: Experimental and numerical study. Energy 2019;187:115941.

[34] Wang C, Zhang Y L. Wave power extraction analysis on a dual-chamber oscillating water column device composed by two separated units: An analytical study. Applied Ocean Research 2021;111:102634.

[35] Sheng W. Motion and performance of BBDB OWC wave energy converters: I, hydrodynamics. Renewable Energy 2019;138:106-20.

[36] Elhanafi A, Macfarlane G, Fleming A, Leong Z. Scaling and air compressibility effects on a three-dimensional offshore stationary OWC wave energy converter. Applied Energy 2017;189:1-20.

[37] Simonetti I, Cappietti L, Elsafti H, Oumeraci H. Evaluation of air compressibility effects on the performance of fixed OWC wave energy converters using CFD modelling. Renewable Energy 2018;119:741-53.

[38] López I, Carballo R, Taveira-Pinto F, Iglesias G. Sensitivity of OWC performance to air compressibility. Renewable Energy 2020;145:1334-47.

[39] Menter F, Kuntz M, Langtry R. Ten years of industrial experience with the SST turbulence model. Turbulence, heat and mass transfer 2003;4:625-32.

[40] Hirt C W, Nichols B D. Volume of fluid (VOF) method for the dynamics of free boundaries. Journal of Computational Physics 1981;39:201-25.

[41] Pecher A, Kofoed J P. Handbook of ocean wave energy. Springer London2017.

[42] Elhanafi A, Fleming A, Macfarlane G, Leong Z. Numerical hydrodynamic analysis of an offshore stationary–floating oscillating water column–wave energy converter using CFD. International Journal of Naval Architecture and Ocean Engineering 2017;9:77-99.

[43] Shalby M, Elhanafi A, Walker P, Dorrell D G. CFD modelling of a small–scale fixed multi–chamber OWC device. Applied Ocean Research 2019;88:37-47.

[44] Fenton J D. A Fifth-Order Stokes Theory for Steady Waves. Journal of Waterway, Port, Coastal, and Ocean Engineering 1985;111:216-34.

[45] Wang C, Zhang Y L. Performance enhancement for a dual-chamber OWC conceived from side wall effects in narrow flumes. Ocean Engineering 2022;247:110552.

[46] Xie N, Hann M, Pemberton R, Iglesias G, Greaves D. A numerical and experimental investigation of the effect of side walls on hydrodynamic model testing in a wave flume. Ocean Engineering 2019;186:106108.

[47] Hadzic H. Development and application of a finite volume method for the computation of flows around moving bodies on unstructured, overlapping grids. 2006;Ph.D.

[48] Chen W, Zhang Y, Yang J, Yu H, Liang S. Experiments and CFD modeling of a dual-raft wave energy dissipator. Ocean Engineering 2021;237:109648.

[49] Elhanafi A, Macfarlane G, Fleming A, Leong Z. Experimental and numerical investigations on the hydrodynamic performance of a floating–moored oscillating water column wave energy converter. Applied Energy 2017;205:369-90.

[50] Xu C H, Huang Z H, Deng Z Z. Experimental and theoretical study of a cylindrical oscillating water column device with a quadratic power take-off model. Applied Ocean Research 2016;57:19-29.

[51] Xu C H, Huang Z H. Three-dimensional CFD simulation of a circular OWC with a nonlinear power-takeoff: Model validation and a discussion on resonant sloshing inside the pneumatic chamber. Ocean Engineering 2019;176:184-98.

[52] Jiang B, Ding J, Wu H, Jiang X, Ye Q, Zhang J. Wave energy resource assessment along Bohai Sea, Yellow Sea, and East China Sea. Acta Energiae Solaris Sinica 2017;38:1711-16.

[53] Leijon M, Waters R, Rahm M, Svensson O, Bostrom C, Stromstedt E, Engstrom J, Rberg S, Savin A, Gravrakmo H, Bernhoff H, Sundberg J, Isberg J, Agren O, Danielsson O, Eriksson M, Lejerskog E, Bolund B, Gustafsson S, Thorburn K. Catch the Wave to Electricity. Ieee Power & Energy Magazine 2009;7:50-54.

753 [54] McIntyre C, Karayaka H B, Adams R, Kaul S, Fahmy J. Analysis of Factors Affecting Peak to Average Ratio
754 and Mean Power in a Slider Crank Wave Energy Converter. 2020 SoutheastCon 2020;1-6.

755 [55] Wang C, Zhang Y L. Hydrodynamic performance of an offshore Oscillating Water Column device mounted
756 over an immersed horizontal plate: A numerical study. Energy 2021;222:119964.

757 [56] Wang C, Xu H, Zhang Y, Chen W. Hydrodynamic investigation on a three-unit oscillating water column array
758 system deployed under different coastal scenarios. Coastal Engineering 2023;184:104345.

DSPACE

https://dspace.org/

Improving wave energy conversion performance of a floating BBDB-OWC system by using dual chambers and a novel enhancement plate

Chen, Wenchuang; Xie, Weixin; Zhang, Yongliang; Wang, Chen; Wang, Liguo ...

2024-05-01
Elsevier
https://doi.org/10.1016/j.enconman.2024.118332
Chen W, Xie W, Zhang Y, et al., (2024) Improving wave energy conversion performance of a floating BBDB-OWC system by using dual chambers and a novel enhancement plate. Energy Conversion and Management, Volume 307, May 2024, Article number 118332

Downloaded from a DSpace repository. https://dspace.org/